J. Fluid Mech. (1995), *vol.* 294, *pp.* 17–46

Turbulent mixed-boundary flow in a corner formed by a solid wall and a free surface

By L. M. GREGA[1], T. WEI[1], R. I. LEIGHTON[2] AND J. C. NEVES[3]

[1] Department of Mechanical & Aerospace Engineering, Rutgers University, Piscataway, NJ 08855-0909, USA

[2] Remote Sensing Division, Naval Research Laboratory, Washington, DC 20375, USA

[3] Center for Computational Sciences and Informantics, George Mason University, Fairfax, VA 03824, USA

(Received 8 April 1994 and in revised form 9 December 1994)

Results from a joint numerical/experimental study of turbulent flow along a corner formed by a vertical wall and a horizontal free surface are presented. The objective of the investigation was to understand transport mechanisms in the corner. Numerical simulations were conducted at NRL to obtain data describing the dynamics of the near corner region. The Reynolds number for the simulations was $Re_\theta \approx 220$. Flow visualization experiments conducted in the Rutgers free surface water tunnel were used to initially identify coherent structures and to determine the effect of these structures on the free surface. Time-resolved streamwise LDA measurements were made for $Re_\theta \approx 1150$. The most significant results were the identification of inner and outer secondary flow regions in the corner. The inner secondary motion is characterized by a weak slowly evolving vortex with negative streamwise vorticity. The outer secondary motion is characterized by an upflow along the wall and outflow away from the wall at the free surface. Additional salient results included observations of surfactant transport away from the surface in cores of vortices connected to the free surface, intermittent energetic transport of fluid to the surface, and attenuation of streak motion by the free surface.

1. Introduction

The structure of two-dimensional turbulent boundary layers has been extensively studied. One important result from this research is the understanding that, although the boundary layer is two-dimensional on the mean, turbulent structure is very three-dimensional. This local three-dimensionality plays a critical role in the dynamics of the flow.

It is interesting, both from a scientific and a technological perspective, to consider effects of three-dimensional boundary conditions on turbulent structure. Consider a turbulent boundary layer formed by horizontal parallel flow of water along a partially submerged vertical solid wall. The free surface in this problem imposes an interesting set of boundary conditions. There is little or no shear at the free surface and spanwise motion (i.e. perpendicular to the free surface) will be strongly attenuated. However, along the solid wall, the flow is constrained by the no-slip condition. Hence, this corner region will be referred to as the mixed-boundary corner.

Mixed-boundary corner flows are relevant in a wide variety of technological problems ranging from sediment and pollutant transport in rivers to ship wake detection. This paper is a report on a joint numerical/experimental investigation into

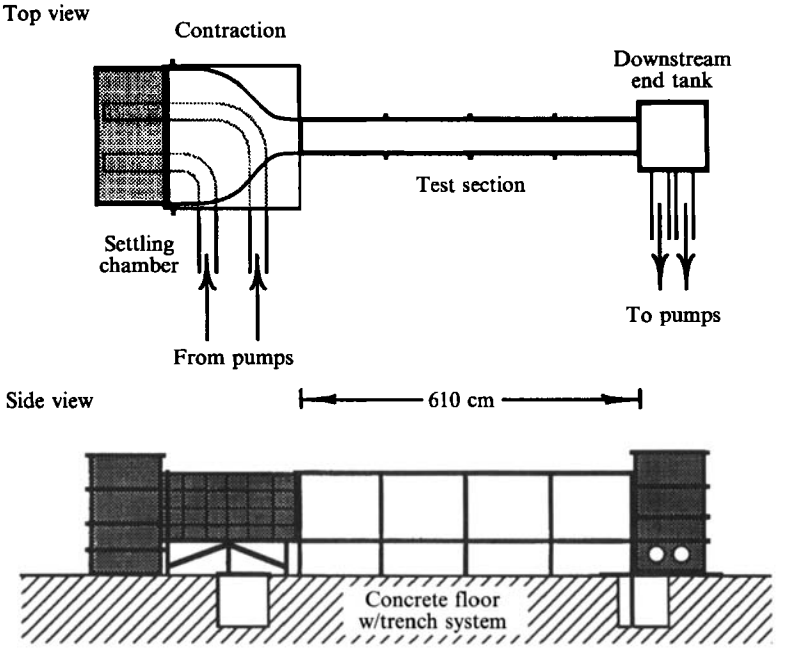

FIGURE 1. Top and side view schematics showing the large free surface water tunnel facility. The test section is 610 cm long, 122 cm deep, and 58 cm wide. Maximum flow rate is 15000 l min^{-1}.

mixed-boundary corner flows. The principal motivation for this work is to develop understanding of transport processes in the corner leading to effective prediction and control algorithms.

1.1. *Literature review*

A good starting point for studying the mixed-boundary corner flow problem is the more thoroughly investigated solid–solid corner problem, such as flow in a rectangular duct. While there are significant differences between the two geometries, research on the solid–solid corner problem has provided valuable insight into the origins of secondary flows.

Schlichting (1979) reports that some of the earliest investigations on solid–solid corner flows were conducted in the 1920s. (Ironically, one of the earliest studies on the mixed-boundary problem was done by Nikuradse at the same time.) The most important result from those early studies was the observation that turbulence transports high-momentum fluid into the corners. This was determined by comparing contours of mean streamwise velocity in a cross-stream plane for laminar and turbulent corner flow. The laminar contours resemble hyperbolas. The mean contours for the turbulent case are wavy lines which appear to oscillate about the laminar contours. In the corner region, the turbulent contours are much closer to the corner than the laminar counterparts.

Nikuradse proposed (according to Schlichting 1979) that high-speed fluid in the corners was the result of the action of a very weak pair of counter-rotating secondary streamwise vortices. The rotation of the vortices advected high-speed fluid from the free stream toward the corner along the angle bisector of the two solid walls. However, it was only much later (Gessner & Jones 1961, 1965; Brundrett & Baines 1964; Perkins 1970; Gessner 1973) that the existence and genesis of the secondary vortices were demonstrated.

Each of these works involved one or more component hot-wire measurements in wind tunnels. One of the experimental difficulties faced by these investigators was that swirl velocities of the secondary vortices were only a few percent (approximately 3% or less) of the mean free-stream velocity. Consequently, their results were highly dependent on the resolution of their hot-wire probes.

Nevertheless, the common conclusion was that weak secondary streamwise vortices result from anisotropy of turbulence in the corner region. This anisotropy is due to curvature of the mean streamwise velocity contours in the corner and leads to production terms in the streamwise vorticity equation. This will be explained in greater detail for the mixed-boundary corner problem in §6.1.

Very little was found in the literature on the mixed-boundary corner. Schlichting (1979) presented data from Nikuradse showing curvature of mean streamwise velocity contours at a free surface. This was modelled by Naot & Rodi (1982). From these works, in combination with results from solid–solid corner research, one can hypothesize the existence of some sort of secondary flow in mixed-boundary corners. However, further investigation is required.

Recently, Stern (1986) and Stern *et al.* (1994) examined the mixed corner problem by towing a surface-piercing flat plate in a water tunnel. However, the principal focus of that work was on wave effects on the boundary layer. As a result, little attention was paid to the secondary flows in the near corner. However, in the most recent work, Stern *et al.* (1994) identified a secondary vortex close to the free surface using a three-component fibre-optic LDA. The vortex is oriented in the streamwise direction with positive vorticity. Because of experimental limitations, measurements could be made no closer than 70 viscous lengths from the free surface; they were unable to resolve the near corner region.

Also lacking are studies of flow structures in the corner region of either the solid–solid corner or the mixed-boundary corner. It should be noted that the seminal work on coherent structures was done by Kline *et al.* (1967); progress since then appears in the review by Robinson (1991). Thus, the absence of structural information on corner flows is probably because much of the corner flow work was done when work on coherent structures was still germinating.

1.2. *Objectives*

The mixed-boundary corner has not been extensively studied. It is an interesting synthesis of turbulent boundary layer and corner flow. A joint numerical/experimental investigation has been initiated to examine this problem. While the ultimate goal is to develop scientifically based prediction and control algorithms, the purpose of this study is to begin understanding the dynamics of the mixed-boundary corner. The specific objectives of this investigation are: (i) to identify principal flow regimes in a mixed-boundary corner; (ii) to identify and characterize important features in each regime; and (iii) to gain insight into the dynamics of the near corner region.

1.3. *A note on coordinates*

In this study, coordinates were chosen such that x, y and z correspond to the stream, free-surface-normal, and wall-normal directions, respectively. The wall-normal coordinate, z, is zero at the wall and increases with distance from the wall. The free surface is located at $y = 0$ with gravity pointing in the negative y-direction. In this right-hand coordinate system, motions toward the free surface are positive, $v > 0$, and depth below the free surface is negative.

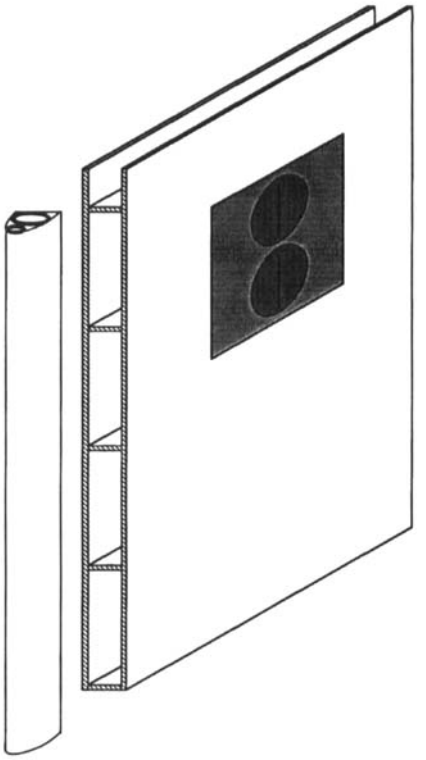

FIGURE 2. Oblique schematic of one section of the test plate. There are a total of six sections. The section shown includes dye injection slots.

2. Experimental apparatus and methods

2.1. *Flow facility*

Experiments were conducted in the free surface water tunnel facility at Rutgers University. Top and side view schematic diagrams of the facility appear in figure 1. The closed circuit tunnel consisted of an upstream settling chamber, two-dimensional contraction, test section, downstream end tank, pumps, and piping. Note that the pumps are not shown in figure 1. Details of the facility may be found in Smith (1992).

Flow was driven by two pumps operating in parallel. Variable-speed controllers were used to set the flow rate between 760 and 15000 l min^{-1}. With the test section completely filled, the maximum flow rate corresponded to a mean free stream velocity of approximately 30 cm s^{-1}.

The upstream settling chamber was 244 cm wide, 122 cm long, and 183 cm deep. Water was pumped into the lower portion of the chamber through two pipe manifolds and passed upward through a sandwich of open-cell foam held by 'egg-crate' lighting panels. The top of the sandwich was aligned with the contraction floor, providing very effective turbulence damping after the inlet manifold.

From the settling chamber, flow passed through a 7.62 cm thick honeycomb flow conditioner which spanned the entrance to a two-dimensional contraction. The contraction was 183 cm long with a 4:1 contraction ratio. It was designed based on the matched cubic splines of Morel (1977) and constructed similar to a boat; thin sheets of PVC were laminated to precisely cut 'ribs'. The relatively long contraction prevented flow disturbance problems (e.g. Görtler vortices, separation) associated with shorter contractions.

The test section measured 58.4 cm in width by 122 cm in depth by 610 cm in length. It was constructed entirely from 1.91 cm thick glass panels placed in a welded steel I-beam frame. Glass was used to provide optical access from all directions.

Finally, a downstream end tank was placed at the exit of the test section. It was similar to the settling tank but only half as wide. A foam/'egg-crate' sandwich which leaned away from the oncoming flow was included for both turbulence damping and wave attenuation.

Flow quality measurements were made in the test section using hot-film anemometry. Two streamwise locations were examined, 76 cm and 533 cm downstream of the test section inlet, at two different centreline velocities, 15 cm s^{-1}, and 21 cm s^{-1}. Twenty-five points in an evenly spaced 5×5 array were used to ascertain flow quality across each cross-section. At the upstream station, flow was uniform across the cross-section to within $\pm 2\%$. (Note that since the variation occurred over more than a metre, the corresponding shear was quite small.) Free stream turbulence levels were on the order of 0.1% of the mean free stream velocity. At the downstream station, sidewall boundary layers were quite large, particularly at the higher flow rate. However, regions of potential flow were frequently observed in the centre of the test section. Again, details of the flow quality measurements appear in Smith (1992).

2.2. *Test plate*

A test plate was constructed to facilitate two-colour laser-induced fluorescence (LIF) flow visualization studies. The plate was an assembly of six rectangular panels made from 1.27 cm thick Plexiglas plates. Each panel was 76 cm long by 122 cm high by 10 cm thick consisting of two vertical parallel faces separated by ~ 7.62 cm wide spacer plates. An oblique drawing of a panel is shown in figure 2. A 2.4:1 (major axis:minor axis) symmetric elliptical leading edge was secured to the upstream end of the test plate; this is also shown in figure 2. The trailing edge of the test plate was left as a blunt square end.

The assembled plate was placed ~ 6 cm from one wall of the test section; the total plate length was 457 cm. Care was taken to minimize discontinuities at the seams of adjacent panels to eliminate wave formation and turbulence generation at the seams. Not only was placement of the individual panels critical, but curvature and variations in thickness of the Plexiglas stock had to be taken into account. The average step height between adjacent panels was less than 0.02 cm. By comparison, one viscous wall unit in this study was ~ 0.01 cm. The largest discontinuity was ~ 0.05 cm at the seam located over 200 cm upstream of the visualization region. To minimize the effect of discontinuities in the plate, PVC tape was placed over each seam.

One of the panels, shown in figure 2, was fitted with two precision machined 12.7 cm long by 0.08 cm wide dye injection slots. The injection slots were housed in a brass insert which was designed so slot positions and orientations could be varied. In this study, the slots were aligned in a vertical line as shown in the figure. Since all of the panels were nominally identical, the panel containing the dye injection slots could be placed anywhere along the plate. In this study, the injection slots were in the fifth panel, 343 cm downstream of the leading edge. Note that slot placement was over 100 cm upstream of the trailing edge, ensuring that wake effects in the visualization region were minimal.

2.3. *Flow visualization*

Shadowgraph and two-colour LIF studies were conducted to examine turbulent structure in the solid wall/free surface corner. Four different viewing orientations of the corner were used including the shadowgraph and three LIF orientations.

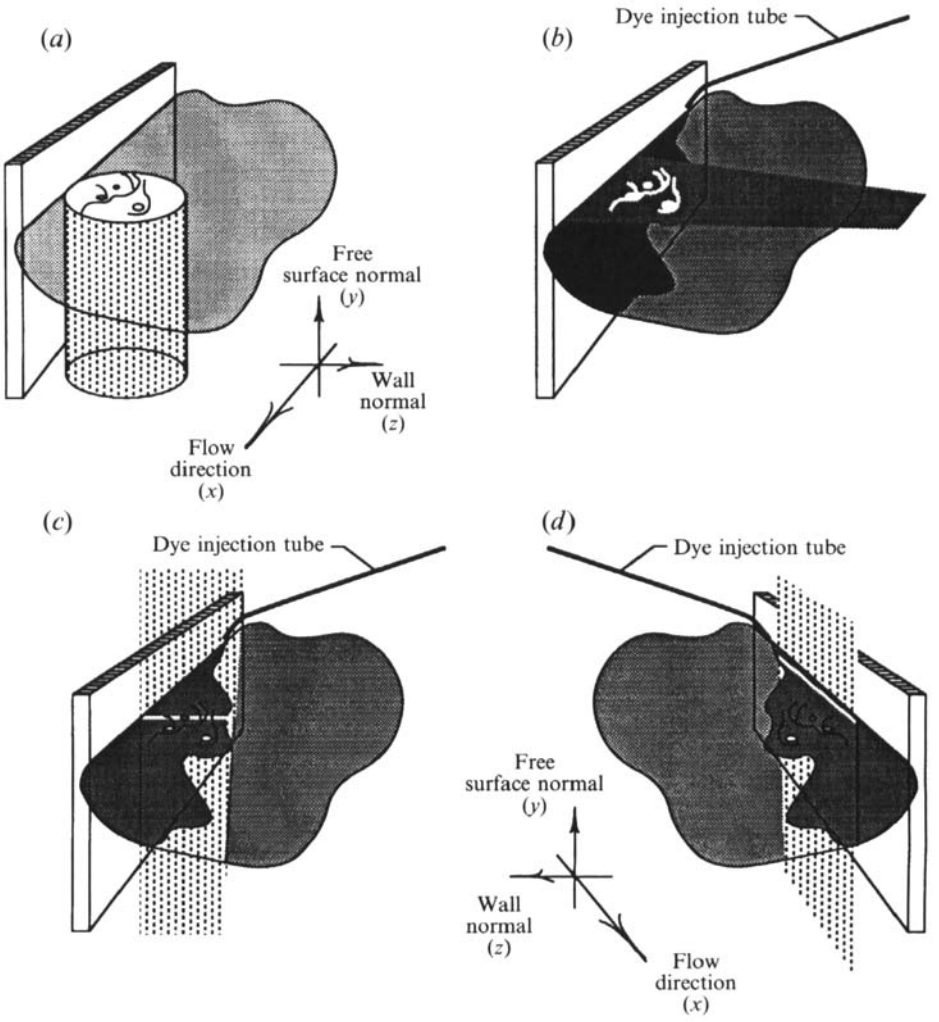

FIGURE 3. Schematic drawings showing the flow visualization orientations: (*a*) shadowgraph of free surface deformations, (*b*) LIF with laser sheet parallel to the free surface, (*c*) LIF with laser sheet perpendicular to the mean flow direction, and (*d*) LIF with laser sheet parallel to the wall.

Schematics of the visualization orientations appear in figure 3. For the LIF studies, dye was injected through vertical wall slots and/or through a 0.08 cm outer diameter stainless steel tube, depending on the phenomenon of interest. Dilute solutions, < 1 p.p.m., of fluorescein (green–yellow) and rhodamine B (orange–red) dyes were used to make the flow.

A 4W all-lines Coherent Innova 70-4 argon-ion laser was used as illumination source for both shadowgraph and LIF experiments. Video records of visualization experiments were generated using a Sony high-resolution video camera (Model DXC-325K), and $\frac{3}{4}$ in. video recording system (Model VO-9600).

Shadowgraphs were made by expanding the laser beam into a 30 cm diameter collimated beam. The expanded beam passed vertically upward through the test section floor and free surface onto a projection screen as illustrated in figure 3(*a*). Free surface deformations due to underlying turbulence appeared as shadows or bright regions on the screen.

Laser sheets for LIF studies were made by using a General Scanning galvanometer (Model G112) to sweep the laser beam. The galvanometer was driven by a sawtooth waveform from a function generator which was synchronized with the framing rate of the video monitor. To minimize beam diameter, and therefore sheet thickness, the laser beam was collimated immediately after exiting the laser; the laser sheet thickness was approximately 0.15 cm, corresponding to roughly 15 viscous units.

Figures 3(*b*)–3(*d*) illustrate positioning of the laser sheet parallel to the free surface, parallel to the wall, and perpendicular to the flow, respectively. For the end views, schematically represented in figure 3(*d*), a plane front surface mirror, measuring approximately 30 cm wide by 35 cm high, was placed in the test section at 45° to the flow. To minimize flow disturbances in the plate wake, the mirror was placed $\sim$ 30 cm downstream of the trailing edge (i.e. $\sim$ 120 cm downstream of the visualization region).

2.4. *Laser Doppler anemometry (LDA)*

Measurements of streamwise velocity were made to develop quantitative understanding of the flow and to validate numerical studies. A commercially available Model 55X LDA optical system from Dantec was used with a 20 mW helium–neon laser light source. The half-angle in water between the two beams forming the measurement volume was $\sim$ 4.9°. This resulted in a measurement volume that was $\sim$ 0.14 cm long and $\sim$ 0.012 cm in diameter (i.e. $\sim$ 13 viscous units by $\sim$ 1.1 viscous units). Flow was seeded with 1.0 μm titanium dioxide particles.

Doppler burst detection and validation was done using a Macrodyne Series 3000 counter processor with interface. With the exception described in the following paragraphs, data analysis was identical to that used by Wei & Willmarth (1989). That is, data rates were sufficiently high to accurately reconstruct time-dependent velocity signals. Raw data traces were reconstructed at even time intervals and digitally filtered using a Gaussian filter with the half-power point set at the viscous frequency. Time-averaged quantities were then computed from the reconstructed filtered time-dependent signals.

When taking measurements far from the wall, light attenuation resulted in a loss of signal strength. As a result, electronic noise would occasionally pass through the various counter processor noise elimination tests and be treated as a 'valid' velocity measurements. This appeared in the raw time-dependent signals as random large-amplitude 'spikes'. It should be noted that the combined duration of all spikes in a signal never exceeded 2% of the total signal.

With the relatively low data rates in the outer flow and the chosen filter cutoff frequency, digital Gaussian filtering would attenuate these spikes, but not remove them completely. It was feared that the remains of the spikes would artificially raise the measured root-mean-square values. To circumvent this problem, an algorithm was developed in which spikes were removed prior to signal processing to enable the digital Gaussian filter to work more efficiently. The spike removal scheme was triggered by stepping through the raw time-dependent velocity signal and keeping a running check on the difference between the 'present' velocity value and the 'previous' value. When this difference exceeded a user-defined threshold, the 'previous' velocity measurement was temporarily stored. The program continued to march forward through the time trace until a local maximum deviation between the present value and the stored value was found. The data between the stored value and the point of maximum deviation were considered to constitute the front half of the spike. The end of the spike was defined to be where the time-dependent velocity trace returned to within a certain percentage of the stored value at the front of the spike. Finally, the velocity

measurements comprising the spike were all set to the stored value and the routine proceeded through the rest of the time trace.

Great care was taken to ensure that the spike removal program did not significantly alter the time-dependent signal. Each time a spike was identified, its duration and location were stored in an output file for subsequent examination. The signal in the vicinity of the longest-duration spikes were examined to verify that the only alteration to the signal was the spike removal. Individual spikes were rarely longer than a few milliseconds in duration. In the worst case, less than ten spikes were detected which were longer than 50 ms. However, no spikes were longer than 100 ms (< 10 viscous timescales) in duration.

2.5. *Experimental conditions*

All flow visualization experiments and LDA measurements were made at a single flow rate; the free-stream velocity was approximately 20.6 cm s^{-1}. Flow visualization was done using the test plate as the vertical wall. The visualization location was $\sim$ 360 cm downstream of the leading edge. LDA measurements were made $\sim$ 400 downstream of the test section inlet using the test section wall opposite the test plate to reduce light attenuation. At that location, the boundary layer was approximately 9.4 cm thick corresponding to a Reynolds number, Re_θ, of roughly 1150.

3. Numerical simulations

3.1. *Geometry*

Simulations were conducted using a modified version of an open channel turbulent flow simulation reported in Handler *et al.* (1993). The ratio of dimensions of the computational domain (streamwise length:depth:half channel width) was 15:6:1. In viscous wall units, this corresponded to $x^+ = 2250$, $y^+ = 900$, and $z^+ = 150$. A schematic drawing of the computational domain appears in figure 4.

The geometry of the mixed-boundary numerical simulation is an idealization of the physical geometry described in §2. A proper and complete numerical treatment of mixed-bounded corner flow implies dealing with four different sets of boundary conditions and two poorly defined corner conditions. The best understood boundary is the no-slip wall. The opposite boundary requires some form of far-field boundary layer approximation, e.g. Spalart & Watmuff (1993), to model the potential core of the channel. The top of the computational domain requires a free surface boundary condition. This condition is complicated by a pair of 'one-dimensional' interfaces between the free surface and the solid wall and between the free surface and the far-field condition. Finally, flow at the fourth boundary, at $y \rightarrow \infty$, must become a canonical two-dimensional boundary layer.

Boundary conditions used the present simulations included: (i) a no-slip vertical wall; (ii) three rigid shear-free symmetry boundaries ($\partial/\partial z = 0$ @ $z^+ = 150$; $\partial/\partial y = 0$ @ $y^+ = 0$ and $y^+ = -900$), (iii) streamwise periodic conditions. The three symmetry conditions were chosen because of specific simplifications at each boundary as described in the following paragraphs.

A definition of the free surface as a rigid shear-free boundary has been used by Lam & Banerjee (1988) and Handler *et al.* (1993) in open channel flow configurations. Rigid shear-free conditions satisfy the free surface boundary conditions in the limit as $Fr \rightarrow 0$. This zero-Froude-number limit is consistent with the experiments where the Froude number was approximately 0.003; there were no waves and surface deformations associated with vortices close to the surface were very small.

Making the bottom of the computational domain a shear-free boundary created a

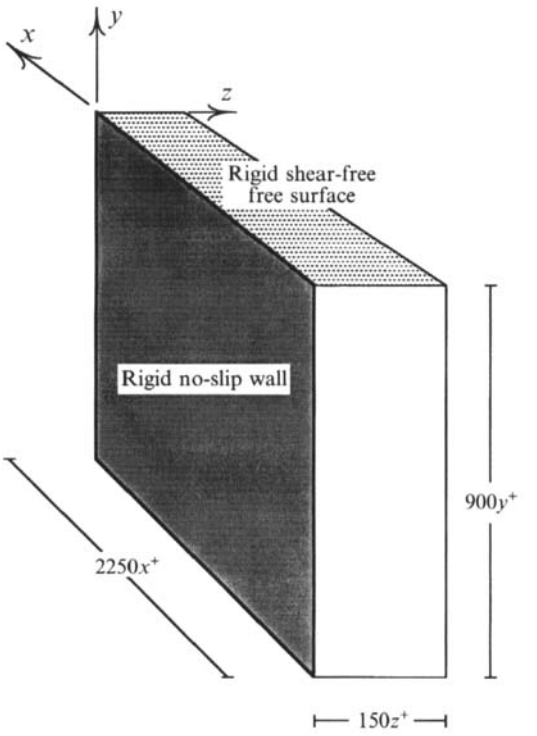

FIGURE 4. Sketch of the computational domain including dimensions in viscous units and boundary conditions. Note that the flow is periodic in the stream direction. $Re_{u_\tau} = 150$; $Re_\theta = 220$.

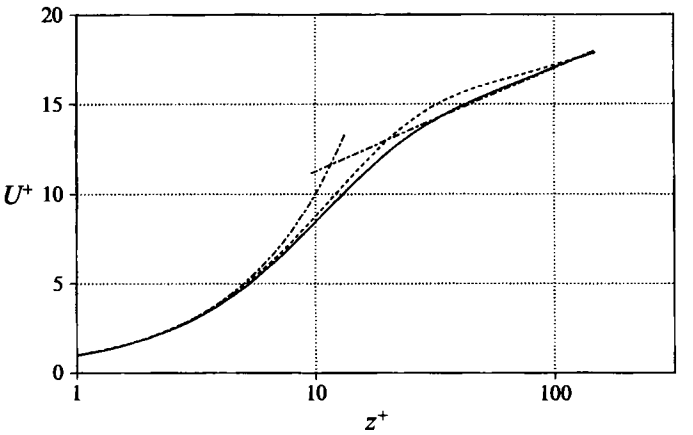

FIGURE 5. Mean streamwise velocity profiles U^+ *vs* z^+, computed from the numerical simulations: ——, averages over the range $-300 > y^+ > -450$; – – –, averages in the region, $-150 > y^+ > -300$; — — —, the canonical law of the wall, $u^+ = z^+$, and log law, $u^+ = 2.5 \log[z^+] + 5.5$.

second modelled free surface from which statistics could be developed. However, this necessitated that the midpoint between the shear-free boundaries, $y^+ = -450$, satisfy the $y \to \infty$ condition. That is, there had to be a two-dimensional canonical flow region at the mid-depth of the domain. This was indeed the case as is shown in the mean streamwise velocity profiles of figure 5. Discussion of the validity of this and other assumptions is deferred to subsequent paragraphs.

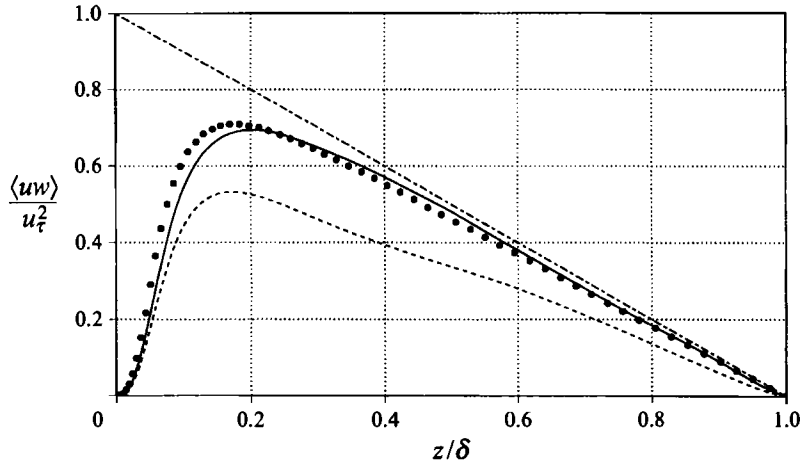

FIGURE 6. Reynolds stress profiles, $\langle uw \rangle / u_\tau^2$ *vs.* z/δ, for the ranges $-300 > y^+ > -450$ (——), and $-150 > y^+ > -300$ (– – –). Solid circles represent data from the turbulent channel flow simulation of Kim *et al.* (1987).

The numerical simulations were intended to replicate the geometry in the experiments where the boundary layer grows in the stream direction. However, computational expediency required modifications at the outer boundary, $z^+ = 150$. In the simulations, the outer boundary condition was defined by requiring the mean flow to be parallel to the wall and the potential outer flow was replaced with a shear free condition. This assumption resulted in turbulence 'filling' the computational domain as the boundary layer grew. Implicit in this assumption was that the physical processes occurring in the outer regions of the flow did not significantly affect the corner.

Perhaps the most stringent condition placed on the three boundaries just described was symmetry. A symmetry boundary is more restrictive than a simple shear-free boundary. The plane of symmetry requires that the flow within the computational domain be perfectly correlated with the image flow and possibly influence the secondary cells forming in the corners.

An *a posteriori* way to test these assumptions is to compare statistics from published results with those obtained from the canonical two-dimensional region using the present code. Figure 5 shows mean velocity profiles, $U(z)$, computed in upper and central regions of the computational domain; i.e. between $-150 > y^+ > -300$, and between $-300 > y^+ > -450$, respectively. Curves plotted in figure 5 were generated by ensemble averaging the streamwise velocity over (x, y)-planes bounded by the full axial length of the domain and y^+ ranges just defined. The friction velocity, however, represents the global value computed using the entire no-slip wall.

The solid line in figure 5 represents the mean profile averaged over the central portion of the domain. The dashed line is the mean profile averaged over an upper portion. The canonical law of the wall, $u^+ = z^+$, and log law, $u^+ = 2.5 \log[y^+] + 5.5$ are plotted as chain-dashed lines for comparison. Observe the close agreement between the solid line and the analytic functions. This is an indication that the flow in the mid-depth region does approach the canonical turbulent boundary layer. Also note the deviation of the dashed line from the canonical boundary layer profile.

Additional evidence supporting the validity of the shear free boundary conditions appears in the Reynolds stress profiles, figure 6. (The reader is reminded that the coordinate system was defined so that w is the wall normal velocity component and

$\langle uw \rangle$ represent turbulent transport of streamwise momentum in the wall normal direction.) Again the solid and dashed lines represent profiles computed from the mid-depth and upper regions of the domain, respectively. Results from Kim, Moin & Moser (1987) are included for comparison. Note that the near-wall behaviour is similar to that in Kim *et al.* (1987); the peak stress is 0.695 located at $z^+ = 30$ in the present computations.

3.2. *Numerical method*

The algorithm used to simulate the flow is a variation of the fourth-order method used by Orszag & Patera (1983) and Kim *et al.* (1987). In those algorithms, the primitive variables were replaced by a fourth-order equation for the wall normal velocity, and a second-order equation for the wall-normal vorticity, by eliminating the pressure field. The remaining components of the velocity field were determined from continuity and the definition of the wall normal vorticity.

By virtue of the boundary conditions described in §3.1, the velocity field was efficiently represented in terms of odd or even Chebyshev polynomials in the wall normal direction, and either sine or cosine functions in the free surface normal direction. Complex trigonometric functions were used in the axial direction. The velocity fields were represented as

$$u(x,y,z) = \sum_{p,\text{even}} \sum_j \sum_k U^*(j,k)\, T_p(y) \cos(k_j z)\, e^{ik_k x}, \tag{1}$$

$$v(x,y,z) = \sum_{p,\text{even}} \sum_j \sum_k V^*(j,k)\, T_p(y) \sin(k_j z)\, e^{ik_k x}, \tag{2}$$

$$w(x,y,z) = \sum_{p,\text{odd}} \sum_j \sum_k W^*(j,k)\, T_p(y) \cos(k_j z)\, e^{ik_k x}, \tag{3}$$

where U^*, V^*, and W^* are the Fourier coefficients.

3.3. *Simulation*

The simulation was started from a random turbulent flow field. It is important to note that the initial flow did not contain secondary mean flows; these developed automatically. After the secondary flows had developed and steady state was achieved, velocity data were obtained for a time span of $800H/U_0$ where U_0 is the initial mean velocity averaged over the far boundary, $z^+ = 150$. This averaging time corresponded to approximately fifty traverses of the computational domain.

Flow inhomogeneities in the corner region generated anisotropic Reynolds stresses and mean secondary flows in planes normal to the mean stream flow. Turbulence statistics of the corner flow are functions of the y- and z-directions. Consequently, ensemble averaging in this flow requires averaging along the x-direction, L_x, and time alone:

$$\langle f \rangle = \frac{1}{NL_x} \sum_n \sum_x f_n(x,y,z). \tag{4}$$

All statistics presented from the simulations were obtained from $N = 210$ statistically uncorrelated flow fields. In addition, the statistical symmetry between the shear-free upper and lower boundaries provide a doubling of the ensemble.

3.4. *Numerical conditions*

As with the experiments, numerical simulations were conducted at a single flow rate. Reynolds number based on momentum thickness, Re_θ, was approximately 220, while Reynolds number based on friction velocity and the width of the computational

domain, Re_τ, was 150. Because of the rigid free surface condition, both the Froude and Weber numbers for this flow are zero.

4. Flow visualization results

A number of flow visualization studies were conducted to gain qualitative physical understanding of the flow. All studies were recorded on $\frac{3}{4}$ in. video tape. Still photographs taken from these video records are presented in this section.

Figure 7 is a single still photograph taken from a shadowgraph study of the near-wall region. A schematic drawing of the visualization orientation is shown in figure 3(*a*); the viewing orientation is down towards the free surface. The wall is located along the bottom edge of the photograph with flow from left to right. The top edge of the photograph is ~ 2900 viscous units ($z \approx 30.5$ cm) away from the wall. Note that the meniscus at the free surface/solid boundary intersection is estimated to be 20 viscous units wide (~ 0.2 cm) and distorts visualization of structures very close to the wall.

Salient features in figure 7 are circular shadows and elongated bright 'ridges. Vortices connected to the free surface cause circular surface depressions, or dimples, due to their low-pressure cores. Collimated light approaching the air–water interface from below is refracted away from the vortex centres resulting in circular shadows. Vortices close to and aligned with the free surface on the other hand, would cause upwellings of fluid. These deformations focus collimated light and create bright ridges in the shadowgraph.

Visual evidence supporting the hypothesis that dark circles are connected vortices was obtained from LIF studies of the free surface. Figure 8 is a sequence of six still photographs taken from a two-colour LIF video sequence of the free surface (i.e. the laser sheet is in the x, z-plane placed at $y^+ = 0$). Flow is again from left to right with the wall aligned with the bottom of the photographs. A schematic of the visualization orientation is shown in figure 3(*b*) with the viewer again looking down at the free surface. Time between successive photographs is 0.33 s ($\Delta t^+ \approx 30$) for a total time of 1.65 s. The top of each photograph is at $z^+ \approx 800$ and the width of each corresponds to about 1680 viscous units.

Rhodamine dye (orange–red) was slowly injected through the vertical dye slot mounted in the test plate. The top of the slot was 130 viscous lengths (1.27 cm) below the free surface. There was no red dye injected directly on the free surface. Simultaneously, fluorescein (yellow–green) dye was injected through a thin 0.08 cm OD stainless steel tube gently placed on the meniscus at the intersection of the free surface and wall. Great care was taken to ensure that the tube did not break through the meniscus. Dye was injected at a very slow flow rate (~ 5 cm^3 min^{-1}) so that it would stay on the surface and not drop below.

It is argued that the fluorescein behaved like a water-soluble surfactant on the free surface. This is because the free surface in the test section was very clean while the surface tension properties of the injected dye were different from the free surface water. In the tunnel, dirt, oils, and other contaminants initially present on the surface advected into the downstream end tank when flow was started. The rate of surface renewal is much slower than the rate at which surface contaminants flow to the downstream end of the test section. Thus, virtually all surface contaminants end up in the downstream end tank and test section exit region. This is supported by the existence of a Reynolds ridge ~ 60 cm upstream of the test section exit; surface contaminants accumulated downstream of the Reynolds ridge while the surface upstream of the ridge was clean.

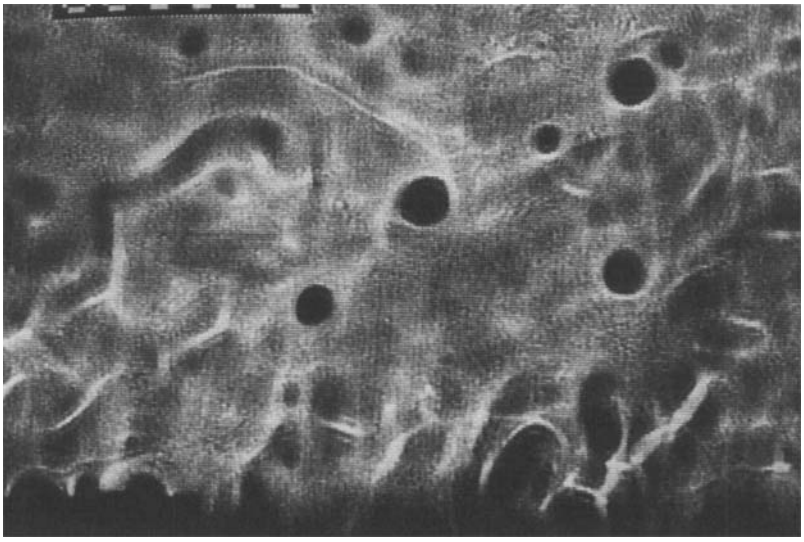

FIGURE 7. Single still photograph taken from a shadowgraph study. Flow is left to right with the wall along the bottom of the photograph.

The surface tension of the fluorescein dye solution would probably be lower than the clean free surface. Consequently, injection of dye on the surface was equivalent to injecting a type of water-soluble surfactant.

If the subsurface and surface flow were steady and laminar, fluorescein dye would spread uniformly across the surface. However, as can be inferred from the shadowgraphs, flow at the surface is turbulent. Surfactants placed on the surface are transported by these turbulent surface motions resulting in a non-uniform distribution of surfactant on the surface.

Non-uniform dispersion of fluorescein (yellow–green) across the free surface is readily evident in figure 8. Flow patterns in the photographs look very similar to two-dimensional side views of an equilibrium turbulent boundary layer. Observe that fluorescein coalesces in and along vortical-shaped structures on the free surface. Note there are bright spots in the centre of vortex cores where dye has concentrated. Except for the vortex cores, very little fluorescein dye is below the surface.

Transport of fluid to the surface was made visible by rhodamine dye. Figure 8 shows a 'burst' of red dye across the surface. Note how red marked fluid from below the surface rises up toward the free surface during the 'burst' and fills in the near-wall region at the surface. It should be kept in mind that very little of the rhodamine actually reaches the surface. When viewed from the side, it was seen that most of the rhodamine spreads away from the wall just below the free surface. Because the laser sheet has a finite thickness, it is impossible to tell from the view in figure 8 how much rhodamine is on the surface and how much is below.

Figure 9 is a four photograph sequence taken from an end view single-colour LIF video sequence. The laser sheet was aligned normal to the stream direction as shown in figure 3(*c*). The wall is along the left-hand side of the photographs; the free surface is along the top. Flow is out of the page toward the reader. The distance from the wall to the right-hand side of the photographs is ~ 385 viscous lengths. The distance from the free surface to the bottom of the pictures is $y^+ \approx -350$. Photographs in figure 9 were taken from successive video frames; the time between photographs is $\Delta t^+ \approx 3$

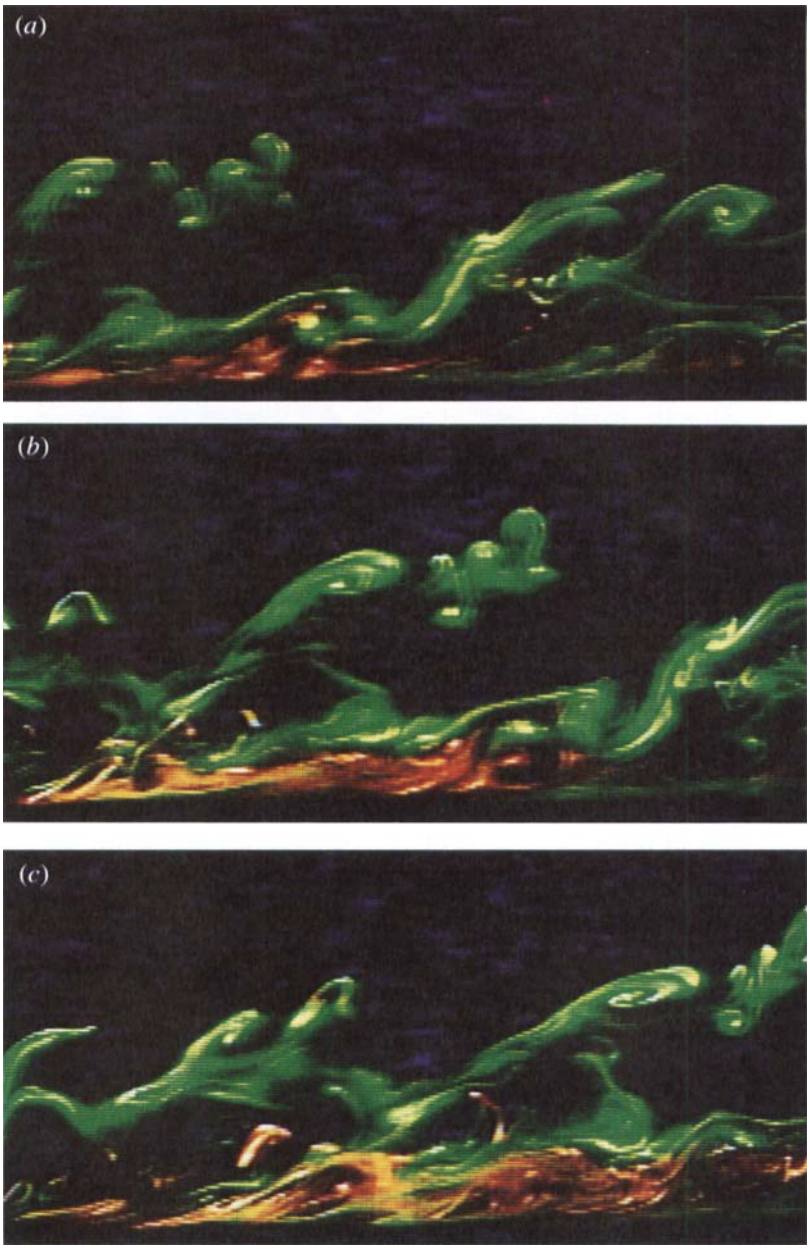

FIGURE 8(*a–c*). For caption see facing page.

(i.e. 0.033 s). As in figure 8, fluorescein dye was injected through a small stainless steel tube onto the free surface.

One important feature in figure 9 is the sudden appearance of fluorescein dye filaments below the surface away from the wall. This can be first seen in figure 9(*b*). A different part of the filament is illuminated in figure 9(*c*). In this case, the filament is located $\sim$ 290 viscous units away from the wall. Since the time between photographs is $\frac{1}{30}$ s, it is clear that the filaments are extremely short in the streamwise direction. Based on the free-stream velocity and the video framing rate, these filaments are

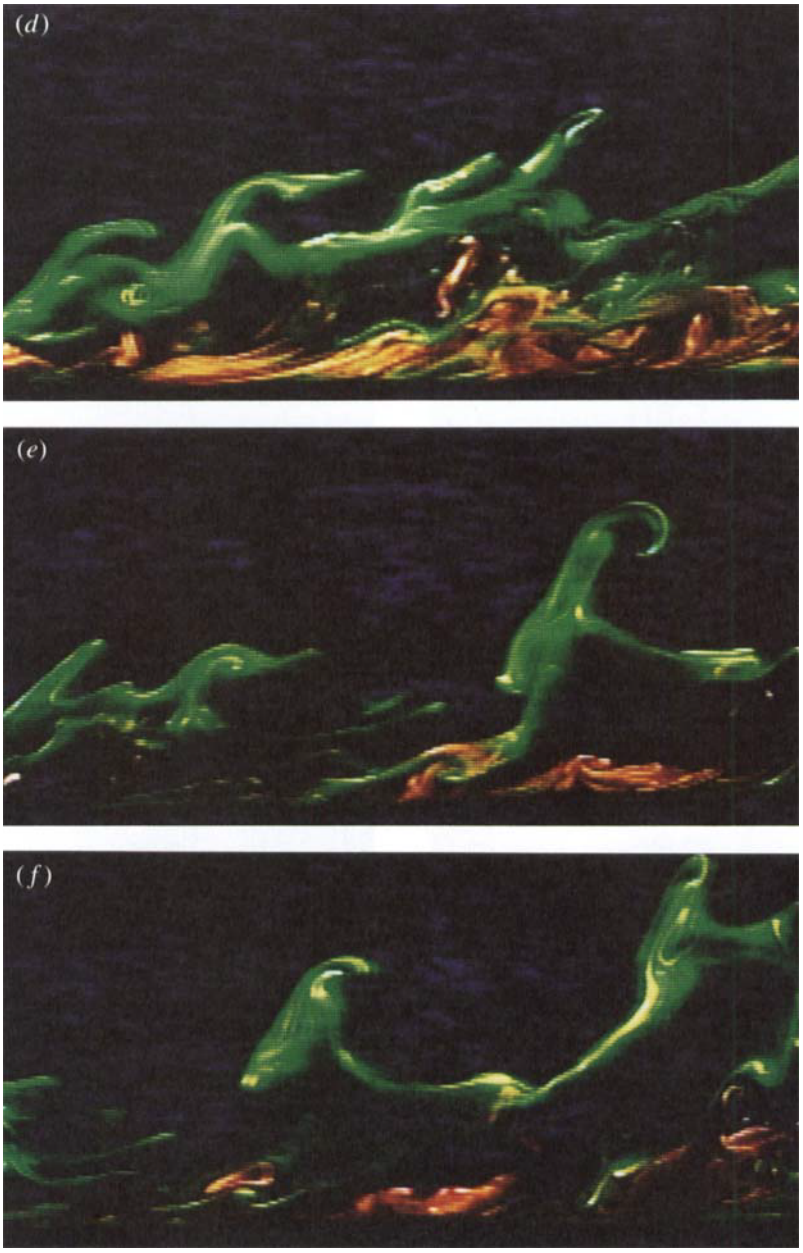

FIGURE 8. Six photograph sequence taken from a two-colour LIF study at the free surface. Flow is left to right. Time between successive photographs is 0.33 s ($\Delta t^+ \approx 30$).

estimated to measure less than 70 viscous units in the stream direction. It is believed that these patterns are created when fluorescein dye is drawn below the free surface through the cores of vortices connected to the surface.

One can deduce a transport mechanism for the removal of surfactant away from the free surface from a combination of figures 7–9. Vortices connected to the free surface draw surface fluid, which may include any contaminants (i.e. surfactants), toward their cores. As soluble surfactant accumulates, it dissolves into the bulk fluid and is drawn

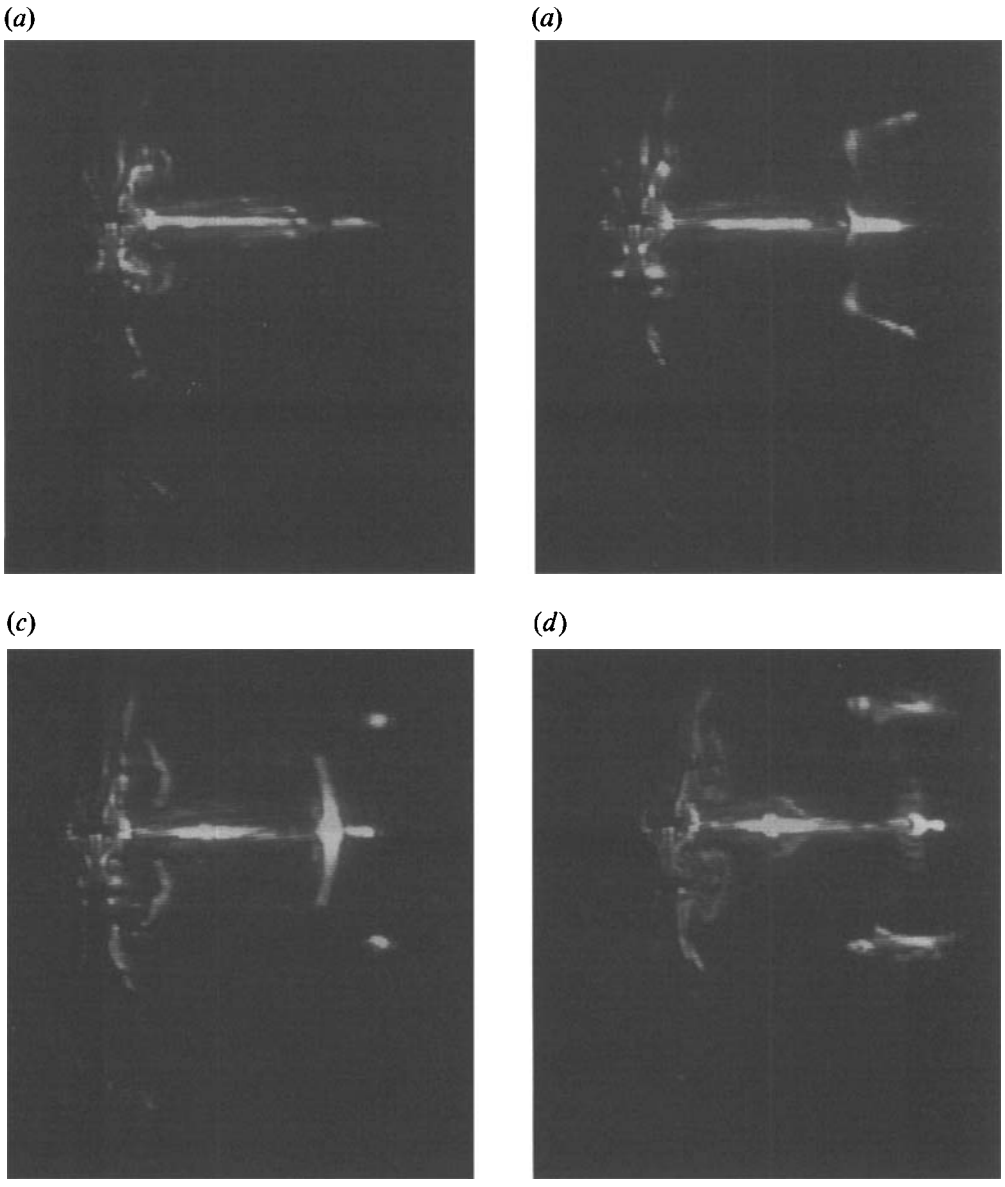

FIGURE 9. Four photograph sequence taken from a single-colour end view LIF video record. Flow is out of the screen. Time between successive photographs is 0.033 s ($\Delta t^+ \approx 3$).

below the surface in the low-pressure cores of the connected vortices. Clearly, as Reynolds number increases and the surface deformations become large, connected vortices will entrain air below the surface as well.

The final LIF orientation was a plain view of the wall, the (x, y)-plane, where the laser sheet was placed flush with the wall, as illustrated in figure 3(*d*). Note that this schematic is oriented differently from the previous three. The viewing orientation is from the left toward the plate. Figure 10 is a single still photograph taken from a two-colour LIF plan view study. Flow is left to right. The free surface is located at the top of the photograph. The width of the pictures corresponds to approximately 1550

viscous lengths in the stream direction. The distance from the free surface to the bottom of the photographs is ~ 470 viscous units.

The principal feature represented in figure 10 is the evolution of turbulent streaks, made visible by rhodamine dye. Dye coalesces into streaks to form bright horizontal lines. It was observed that the streak closest to the free surface appeared to remain parallel to the free surface while streaks further below the surface tended to meander much more.

To better quantify this observation, mean streak location relative to the free surface was measured. This is shown in figures 11–13. Data were obtained by examining 120 still frames from a single-colour plan view LIF video sequence, similar to figure 10. Every twentieth video frame in the sequence was used for a total averaging time of $T^+ \approx 6115$. For each frame, a clear film was placed over the video screen. The free surface and all visible low-speed streak positions were marked. The same streamwise location on the television screen was used for every measurement. Mean streak spacing, λ, and distance from the free surface, y, were non-dimensionalized by the friction velocity measured close to the free surface (cf. §5.2) and kinematic viscosity.

Figure 11 is a plot of the time-dependent positions of six streaks. The ordinate is distance below the free surface in viscous units where $y^+ = 0$ corresponds to the free surface. The abscissa is viscous time units. Note the correlation between streak motions close to the surface and farther away. 'Fronts' can be observed as streaks move toward and away from the surface. The apparent correlation between at least six streaks close to the free surface is in marked contrast to the spanwise correlation of turbulence in the two-dimensional equilibrium boundary layer. Numerous studies, including McLean (1990), have shown that near-wall turbulence becomes uncorrelated within 100–200 viscous units in the spanwise direction. That is, in a canonical boundary layer, the motion of a given streak will have some effect on the evolution of adjacent streaks, but there will be little effect on fluid motions several hundred viscous spanwise units away.

The principal difference between wall streaks close to and far from the free surface is the amplitude of their spanwise motion. The streak closest to the free surface is necessarily restricted from meandering, particularly toward the surface, while streaks further from the surface are increasingly unrestrained. This can be seen in figure 12 which shows probability density functions for the first, third, and fifth streaks (counting from the free surface down). Comparison of widths of the p.d.f.'s clearly illustrates that the amplitude of spanwise motions increases with distance from the surface.

There also appears to be an increase in streak spacing with increasing distance from the surface. To demonstrate this, a p.d.f. of mean streak spacing close to the surface was generated and compared to the two-dimensional equilibrium turbulent boundary layer results of Johansen & Smith (1986). This appears in figure 13. Johansen & Smith (1986) used hydrogen bubble flow visualization techniques to study boundary layer control with riblets. Their method of measuring streak spacing was similar to that used here. Data for near-surface streak spacing were obtained by measuring instantaneous separations between the three streaks closest to the free surface. Present streak spacing measurements appear in figure 13 as a grey shaded region while the canonical boundary layer (without riblets) results of Johansen & Smith (1986) are shown as a heavy solid line. Note that the near-surface streak spacing is smaller on the mean than the two-dimensional equilibrium counterpart. In addition, the near-surface p.d.f. is narrower, demonstrating that the free surface inhibits spanwise motions.

FIGURE 10. Single photograph taken from a two-colour LIF video sequence in which the laser sheet is flush with the wall.

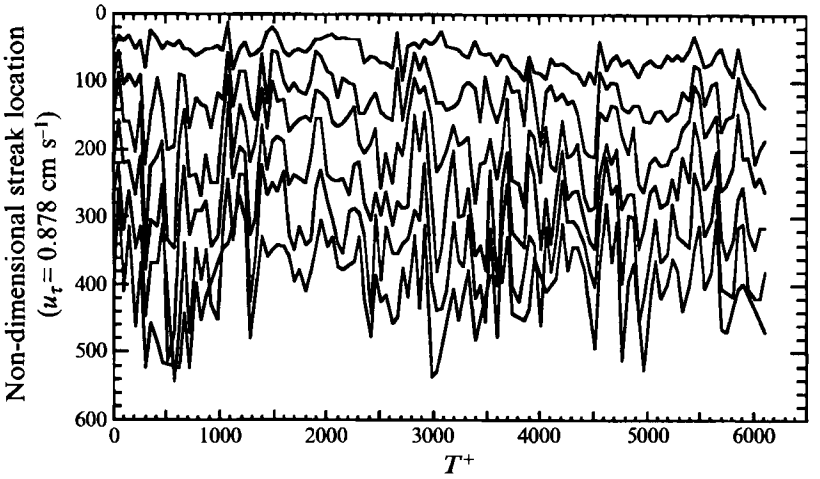

FIGURE 11. Plot of streak location as functions of time for the six streaks closest to the surface. Data are non-dimensionalized by kinematic viscosity and friction velocity close to the free surface.

5. Turbulence statistics

Mean and fluctuating statistics, primarily from the numerical simulations, are presented in this section. Because of symmetry of the averaged fields, only the upper half of the computational domain is shown, i.e. in the range $0 > y^+ > -450$. Details of the simulation and flow conditions were presented in §3.

In addition, streamwise velocity LDA data from four streamwise velocity profiles are presented. In all cases, measurements were made in the tunnel sidewall boundary layer approximately 400 cm downstream from the test section inlet. Average data rates were greater than the viscous frequency, u_τ^2/ν, which enabled reconstruction of time-dependent velocity signals. Sampling times exceeded 6 min ($T^+ > 36000$) to ensure accurate averages.

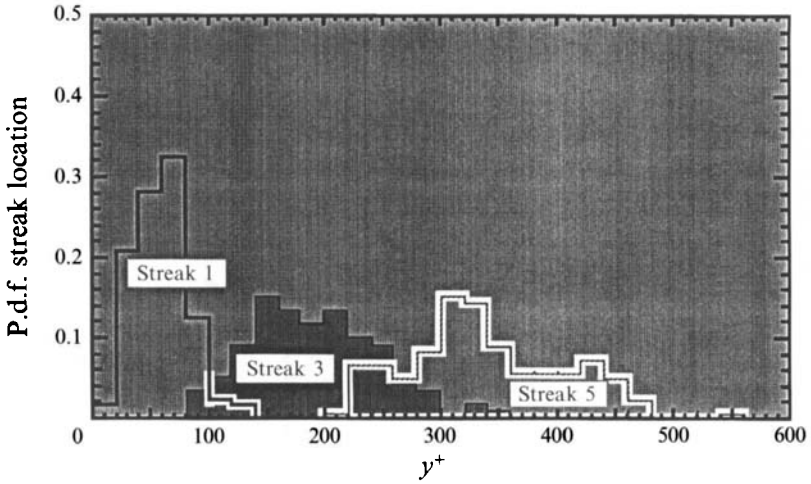

FIGURE 12. Probability density distributions of streak location for the first, third, and fifth streaks (counting down from the free surface). Note the broadening of p.d.f.'s with increasing distance from the surface.

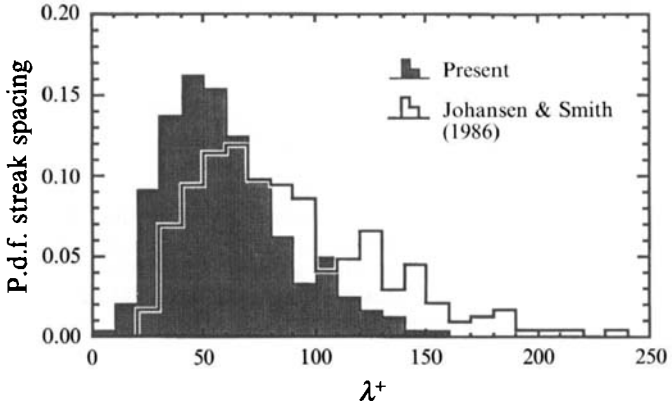

FIGURE 13. Probability density distributions of streak spacing for the three streaks closest to the free surface, and in a canonical boundary layer from Johansen & Smith (1986).

5.1. *Numerical results*

Mean velocity contours obtained from the numerical simulations are shown in figure 14. All three velocity components are plotted in the (y, z)-plane. The mean axial velocity, U, free surface normal velocity, V, and wall normal velocity, W, appear in figure 14(*a–c*), respectively. In each case, velocities are normalized by U_0, the initial velocity at the far boundary, $z^+ = 150$. The no-slip wall appears at the left of each plot, and the free surface is at the top.

Three regions can be identified from the mean velocity contours in figure 14. An 'inner' secondary cell resides in the region $0 > y^+ > -100$. In the region $-50 > y^+ > -300$, there is a larger, but weaker, cell which will be referred to as the 'outer' secondary cell. Finally, far below the free surface, $-300 > y^+ > -450$, there is a canonical turbulent boundary layer region. To aid in visually identifying these regions, mean cross-stream velocity vectors are included in figure 14(*a*). Note that the

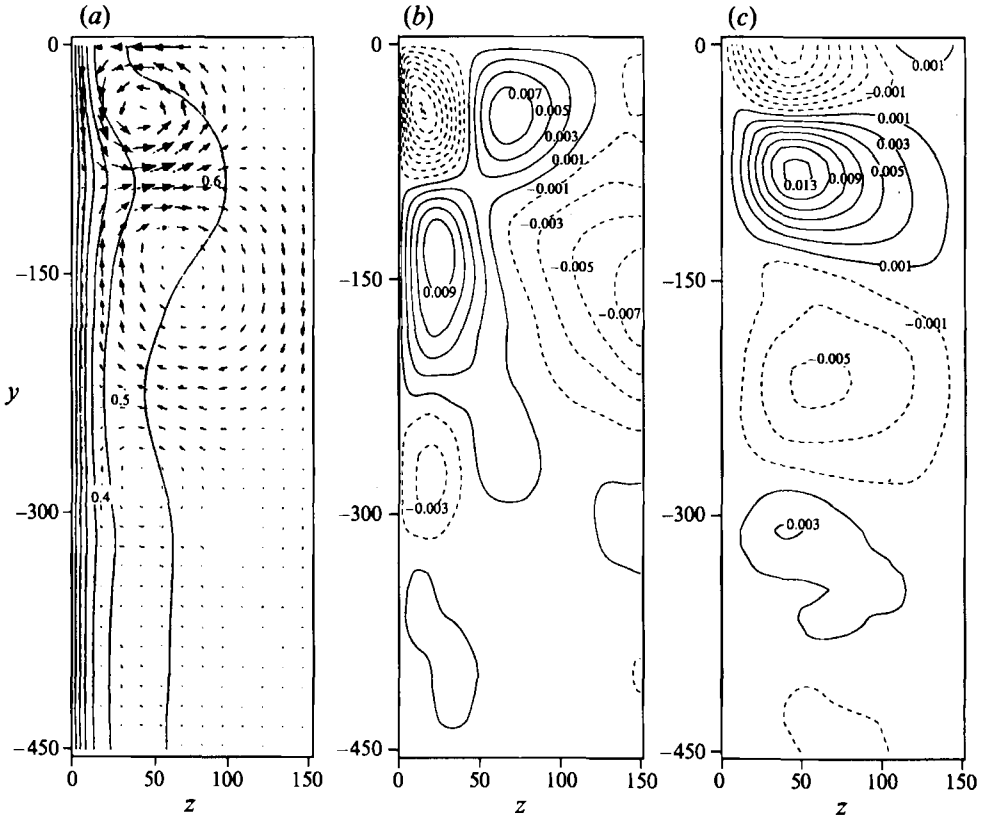

FIGURE 14. Mean velocity distributions taken from the numerical simulations. Positive and negative contours appear as solid and dashed lines, respectively. (*a*) $0.68 \leqslant U/U_0 \leqslant 0$; contour increments are 0.10. The arrows are local mean cross-stream velocity vectors. (*b*) $0.0106 \leqslant V/U_0 \leqslant -0.0148$ with increments of 0.002. (*c*) $0.0143 \leqslant W/U_0 \leqslant -0.0126$ with increments of 0.002. In each figure, the wall is the left boundary and the free surface is the top boundary.

longest arrow corresponds to $\sim 2\%$ of the mean stream velocity. This is consistent with observed magnitudes of cross-stream velocities in square ducts.

The mean free-surface-normal velocity, shown in figure 14(*b*), is zero both at the free surface, owing to the no-flow requirement, and at the solid wall owing to the no-slip condition. The condition on the normal velocity at the far boundary, $z^+ = 150$, is that $\partial V/\partial z = 0$. Near the corner, $y^+ \approx -50$, $z^+ \approx 16$, the vertical velocity achieves its maximum amplitude, $V_{max}/U_0 = -0.015$; $V_{max}/U_{max} \approx -0.22$.

The wall normal velocity, W, shown in figure 14(*c*), must be zero at the wall and at the far boundary, $z^+ = 150$. There are no restrictions on W at the free surface where a current toward the wall exists. Below this, around $y^+ = -85$, $W_{max}/U_0 = 0.016$; $W_{max}/U_{max} \approx 0.023$.

Turbulence intensities, or normal stresses, u', v', and w', are shown in figure 15(*a–c*), respectively. In these figures, normal stresses were normalized by the friction velocity computed from the mean wall shear stress. Like figure 14, the wall appears at the left of each plot, the free surface is at the top, and the mid-depth of the domain is shown at the bottom.

The normal stress distributions exhibit three regions similar, but not identical, to the mean flow distributions shown in figure 14. There is a region $0 > y^+ > -70$ where there

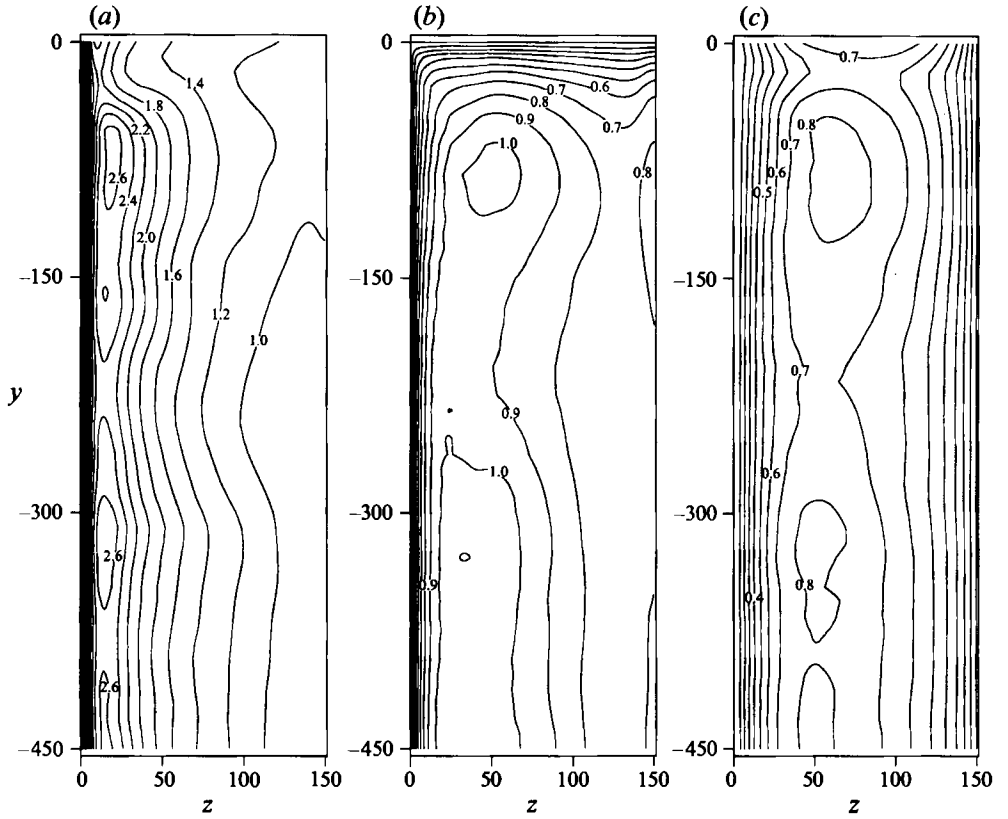

FIGURE 15. Turbulent normal stress distributions taken from the numerical simulations. (*a*) u'/u_τ; maximum contour is 2.83, contour increment is 0.20. (*b*) v'/u_τ; maximum is 1.10, increments are 0.10. (*c*) w'/u_τ; maximum is 0.83 with increments of 0.10. In each figure, the wall is the left boundary and the free surface is the top boundary.

are large deviations from the canonical r.m.s. profiles. Farther from the free surface, $-70 > y^+ - 300$, deviations from the canonical profiles are smaller but non-zero. Finally, in the centre of the domain, $-300 > y^+ > -450$, the normal stress distributions are very similar to the canonical profiles.

The turbulent shear stresses, Reynolds stresses, are shown in figure 16 normalized by u_τ^2. Note that the contours in figure 16 are not as smooth as previous statistics. This is because Reynolds stresses are higher-order moments which require larger statistical samples to obtain good convergence. In this problem, the two inhomogeneous directions limit the size of the statistical sample. However, doubling the ensemble did not significantly alter the turbulent shear stress statistics. Therefore, it is argued that figure 16 exhibits the main features of the turbulent shear stress distributions.

In the corner region, $\langle uv \rangle$, which represents turbulent transfer of streamwise momentum in the free surface normal direction, is of the same magnitude as $\langle uw \rangle$. However, far from the free surface, turbulent transport of streamwise momentum in the wall normal direction, $\langle uw \rangle$, is much greater than either $\langle uv \rangle$ or $\langle vw \rangle$. The distribution of $\langle uw \rangle$, shown in figure 16(*b*), is qualitatively similar to the distributions of normal stresses, u' and w', shown in figures 15(*a*) and 15(*c*). The remaining component of the Reynolds stress tensor $\langle vw \rangle$, is approximately an order of magnitude

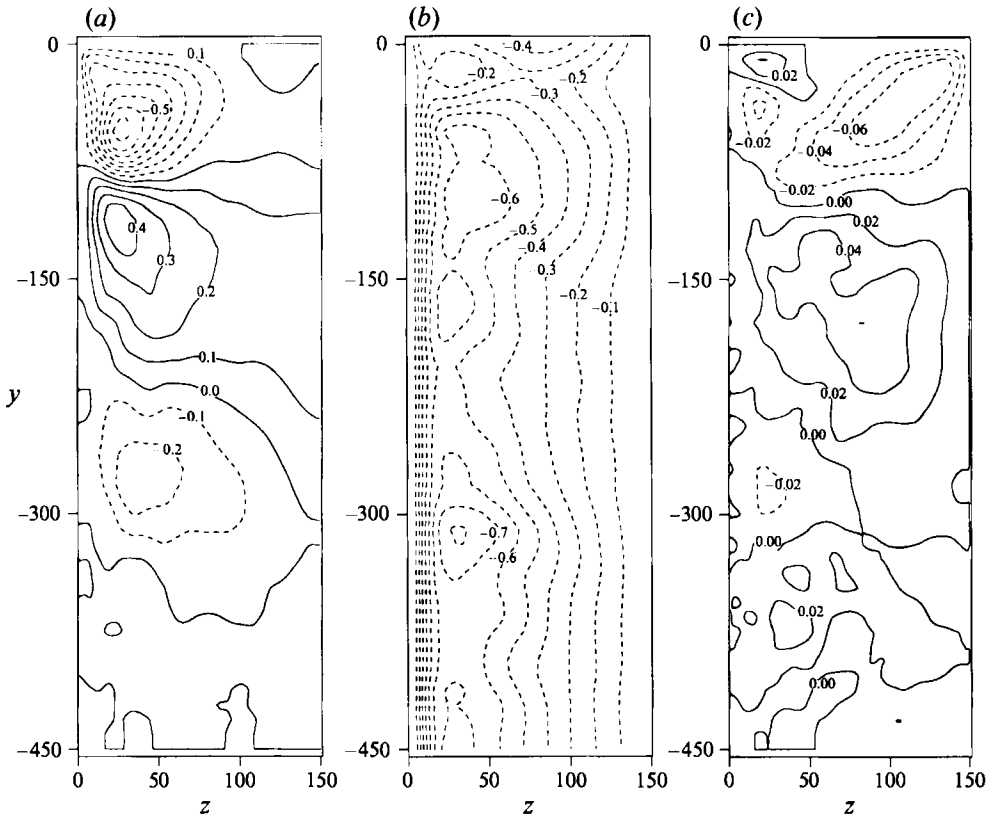

FIGURE 16. Reynolds stress distributions from numerical simulations. (*a*) $0.47 \leqslant \langle uv \rangle / u_\tau^2 \leqslant -0.71$; contour increment is 0.10. (*b*) $3.4 \times 10^{-4} \leqslant \langle uw \rangle / u_\tau^2 \leqslant -0.83$; increments are 0.10. (*c*) $0.053 \leqslant \langle vw \rangle / u_\tau^2 \leqslant -0.079$; increments are 0.02. Positive and negative contours appear as solid and dashed lines, respectively. In each figure, the wall is the left boundary and the free surface is the top boundary.

smaller than the other components over the entire domain. This is consistent with Reynolds stress data from solid–solid corner flows.

Mean and fluctuating pressure distributions, shown in figure 17, also exhibit several distinct regions. Mean pressure distributions normalized by ρU_0^2 appear in figure 17(*a*) while fluctuating pressure statistics were normalized by ρu_τ^2 and are presented in figure 17(*b*). Close to the free surface, there are mean pressure maxima in the corners and a low-pressure region around $y^+ = -100$. The low pressure may be interpreted as related to the secondary cells while high pressure in the corners is consistent with the idea that the corners are stagnation points for the secondary cells.

5.2. *Experimental results*

Two $U(z)$ profiles and two $U(y)$ profiles from single-component LDA experiments are presented in figures 18 and 19 for comparison. In figure 18, two mean $U(z)$ profiles measured at different distances from the free surface are compared to the canonical mean profile compiled by Coles (1953). Squares denote data taken close to the free surface ($y^+ \approx -60$) while circles are data taken at the tunnel centre height ($y^+ \approx -5080$). The line passing through the data is Coles' profile. Friction velocity, u_τ, and wall location, $z^+ = 0$, were determined by fitting $U(z)$ data to the solid line.

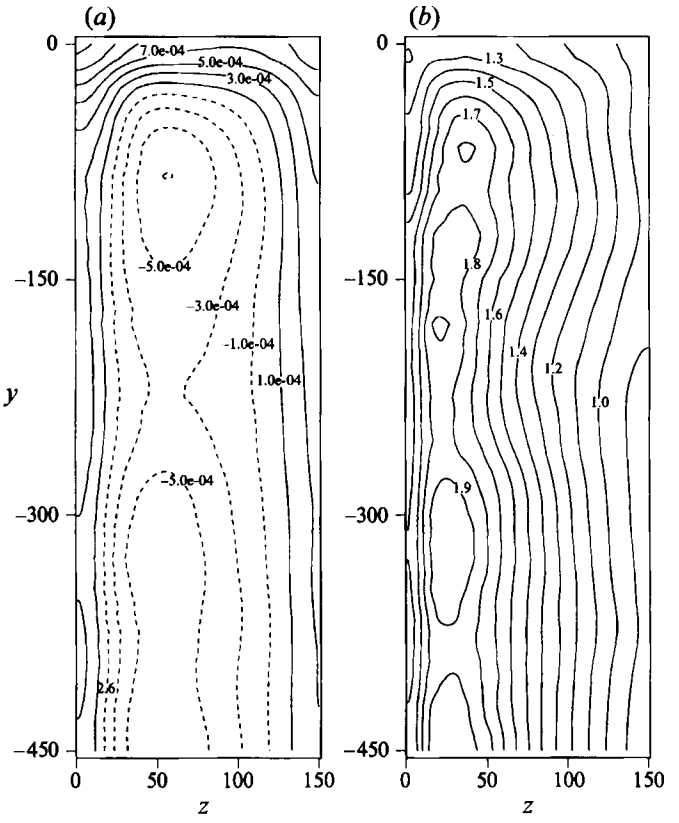

FIGURE 17. Mean and fluctuating pressure contours. (*a*) $3.4 \times 10^{-4} \leqslant P/\rho U_0^2 \leqslant -7.0 \times 10^{-4}$; contour increment is 2.0×10^{-4}. (*b*) $1.98 \leqslant p'/\rho u_\tau^2 \leqslant 0.87$; increments are 0.10.

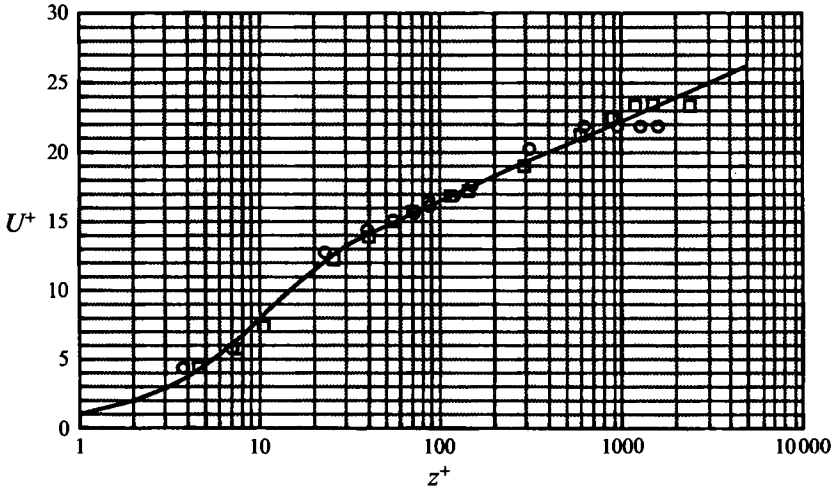

FIGURE 18. Mean streamwise velocity profiles taken in the wall-normal direction: ○, data taken in a two-dimensional canonical boundary layer; □, data taken 0.635 cm from the free surface ($y^+ \approx -60$).

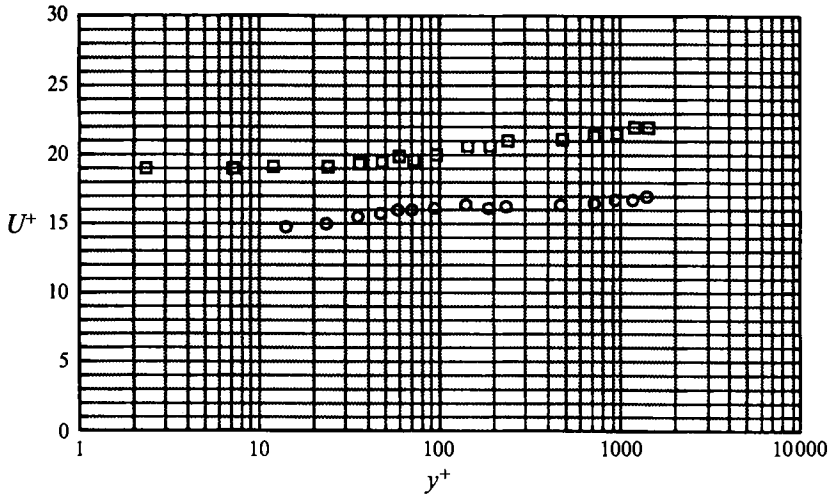

FIGURE 19. Mean velocity profiles taken in the free-surface-normal direction: ○, data taken 1.35 cm from the wall ($z^+ \approx 130$); □, data taken at $z = 6.08$ cm ($z^+ \approx 585$).

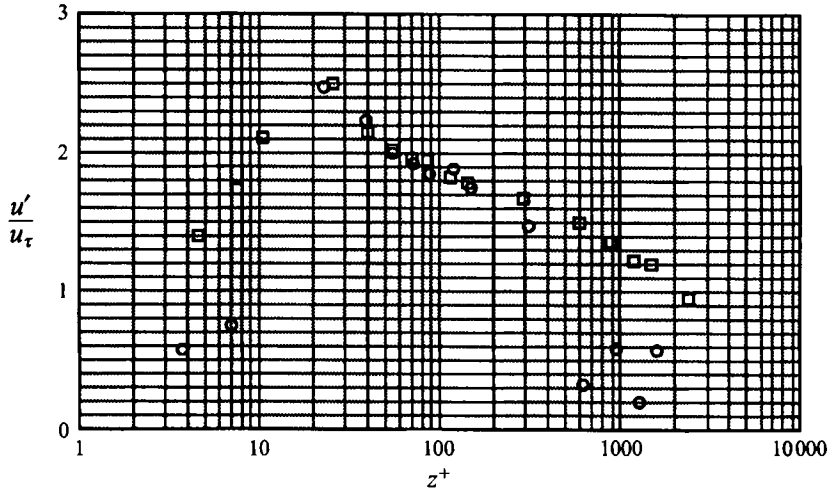

FIGURE 20. Streamwise turbulence intensity non-dimensionalized by friction velocity plotted versus non-dimensional distance from the wall: ○, data taken in a two-dimensional canonical boundary layer; □, data taken 0.635 cm from the free surface ($y^+ \approx -60$).

The first discernible difference between the profiles is that friction velocity decreases near the surface. The friction velocity was 0.878 cm s^{-1} at $y^+ \approx -60$ and 0.944 cm s^{-1} far below the free surface. This is consistent with numerical results in figure 14(*a*) which show boundary layer thickening due to outflow from the inner secondary cell.

The second observation is that the boundary layer is roughly twice as thick at the free surface than far below. This can be seen by comparing locations in the two profiles of figure 18 where the mean velocity first appears to reach a constant maximum value. For instance, the last four points in the tunnel centre height profile are approximately equal; the first of these points is located at $z^+ = 600$. In contrast, the mean profile close to the surface does not reach a maximum until $z^+ \approx 1200$.

Dependence on depth are also noticeable in the two $U(y)$ profiles shown in figure 19.

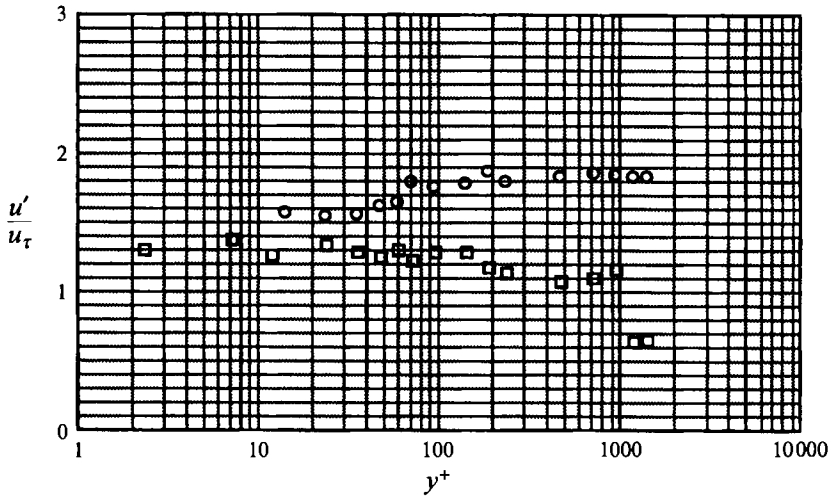

FIGURE 21. Streamwise turbulence intensity non-dimensionalized by friction velocity plotted versus non-dimensional distance from the free surface: ○, data taken 1.35 cm from the wall ($z^+ \approx 130$); □, data taken at $z = 6.08$ cm ($z^+ \approx 585$).

Circles and squares represent data taken at $z^+ \approx 130$ and 585, respectively. This figure clearly shows a reduction in the mean velocity as the free surface is approached. It should be noted that the friction velocity values used in the two vertical profiles were obtained by taking a coarse horizontal $U(z)$ profile at $y^+ \approx -1450$ (15.24 cm below the free surface). From this profile, u_τ and wall location were determined by fitting to the Clauser plot. In the $z^+ = 130$ profile, u_τ was found to be 0.925 cm s^{-1}. In the $z^+ = 585$ profile, u_τ was determined to be 0.935 cm s^{-1}. These values compare well with the value of 0.944 cm s^{-1} obtained at the tunnel centre height.

Time averages of fluctuating streamwise velocity, u', were computed from the LDA data. Figure 20 shows a plot of $u'(z)$ obtained at $y^+ = -60$ and -5080 (plotted as squares and circles, respectively); u' is non-dimensionalized by the appropriate friction velocity, u_τ. Comparison of the two profiles shows that in the near-wall region, $z^+ < 20$, the value of u' at $y^+ = -60$ is significantly greater than its counterpart measured at $y^+ = -5080$. Farther away from the solid wall, $z^+ > 200$, streamwise fluctuations are again larger near the free surface than in the canonical turbulent boundary layer.

To further examine variations of turbulence properties with distance from the surface, u' was measured as a function of channel depth. In figure 21, u' is again normalized by friction velocity and circles and squares represent data from $z^+ \approx 130$ and 585 profiles, respectively.

6. Discussion

The results of this investigation and the conclusions drawn from works on solid–solid corner flows indicate that the mixed-boundary corner may be divided into three regions shown schematically in figure 22. There is an 'inner secondary region', characterized by a weak streamwise vortex. An 'outer secondary region' originates at the wall below the inner secondary region and extends around the inner secondary cell to the free surface. At the free surface, the outer secondary flow leads to a thickening of the boundary layer. Finally, there is a two-dimensional equilibrium region far from

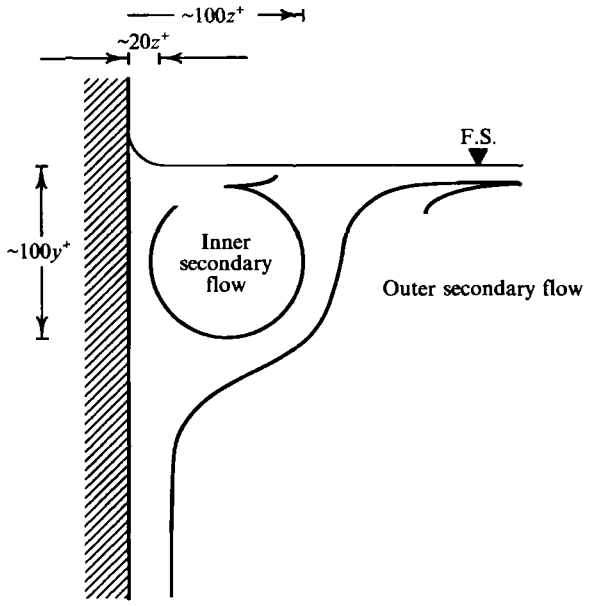

FIGURE 22. Schematic drawing showing the hypothesized inner and outer secondary regions in a mixed-boundary corner. Far from the free surface, flow is expected to approach the canonical turbulent boundary layer.

the free surface. The objective of this discussion is to present physical arguments to explain the origin of the hypothesized secondary flows.

6.1. *The inner secondary vortex flow*

The 'inner secondary vortex' in the near corner is driven by the anisotropy in the local turbulent shear stresses. This is analogous to the mean streamwise vorticity generated by turbulence in a solid–solid corner. Physical arguments are presented here based on the governing equations of motion and compared to present results.

Consider the instantaneous turbulent momentum equations:

$$\mathrm{D}U_i/\mathrm{D}t = -(1/\rho)(\partial P/\partial x_i) + \nu\nabla^2 U_i. \tag{5}$$

Note that U_i and P are the Reynolds decomposition, i.e. the sum of mean and fluctuating parts, of velocity and pressure. Taking the curl and then the mean of (5) yields a set of equations describing mean vorticity transport in the flow. In this case, the mean streamwise vorticity equation is of particular interest:

$$\frac{\mathrm{D}\Omega_x}{\mathrm{D}t} = \Omega_x\frac{\partial U}{\partial x} + \Omega_y\frac{\partial U}{\partial y} + \Omega_z\frac{\partial U}{\partial z} + \nu\nabla^2\Omega_x$$
$$+ \frac{\partial}{\partial x}\left(\frac{\partial\langle uv\rangle}{\partial z} - \frac{\partial\langle uw\rangle}{\partial y}\right) + \frac{\partial^2}{\partial y\,\partial z}(\langle v^2\rangle - \langle w^2\rangle) + \left(\frac{\partial^2}{\partial z^2} - \frac{\partial^2}{\partial y^2}\right)\langle vw\rangle, \tag{6}$$

where $\Omega_x = \partial W/\partial y - \partial V/\partial z, \Omega_y = \partial U/\partial z - \partial W/\partial x, \Omega_z = \partial V/\partial x - \partial U/\partial y$, and $\langle\,\rangle$ denote time-averaged quantities.

The left-hand side of (6) describes the rate of change of vorticity following a fluid element relative to an inertial reference frame. The first three terms on the right-hand side represent vortex stretching or the interaction of mean vorticity with mean velocity gradients. The second and third terms in particular represent stretching and

reorientation of cross-stream vorticity into the stream direction by mean shear. The fourth term in (6) is the diffusion of vorticity due to viscosity. The remaining terms are vorticity production terms resulting from turbulent fluctuations. Observe that if turbulence is isotropic, these terms reduce to zero.

If one assumes a steady flow, $\mathrm{D}/\mathrm{D}t = 0$, in which streamwise gradients are small, $\partial/\partial x \approx 0$, then

$$\Omega_y \partial U/\partial y + \Omega_z \partial U/\partial z \approx (\partial U/\partial z)(\partial U/\partial y) - (\partial U/\partial y)(\partial U/\partial z) = 0. \tag{7}$$

The two vorticity reorientation terms cancel and the mean streamwise vorticity equation reduces to

$$0 = (\partial^2/\partial y\,\partial z)(\langle v^2\rangle - \langle w^2\rangle) + (\partial^2/\partial z^2 - \partial^2/\partial y^2)\langle vw\rangle + \nu(\partial^2\Omega_x/\partial y^2 + \partial^2\Omega_x/\partial z^2). \tag{8}$$

It should be noted here that the assumption of zero streamwise gradients, $\partial/\partial x$, is exactly true in the numerical simulations, but it is not strictly correct for the growing boundary layer studied in the experiments; it may not be possible to simply ignore all terms in which derivatives with respect to x appear. The validity of this assumption must be investigated.

It is possible to further simplify (8) by noting that $\langle vw\rangle$ is either zero or negligibly small everywhere in the flow. Reynolds stress statistics obtained from the simulation, figure 16(*c*), indicate that $\langle vw\rangle$ is everywhere an order of magnitude smaller than either $\langle uw\rangle$ or $\langle uv\rangle$. This can be deduced from physical arguments as well. Far from the surface there is no mean spanwise momentum transport. This means that v- and w-fluctuations are uncorrelated and $\langle vw\rangle$ is exactly zero. Close to the free surface, at the very low Froude numbers examined in both experiments and numerical simulations, both wall normal and streamwise fluctuations are significantly increased but the free surface normal fluctuations are strongly attenuated. Consequently $\langle vw\rangle$ is also small. Therefore, (8) further simplifies to

$$0 = (\partial^2/\partial y\,\partial z)(\langle v^2\rangle - \langle w^2\rangle) + \nu(\partial^2\Omega_x/\partial y^2 + \partial^2\Omega_x/\partial z^2). \tag{9}$$

The first term in (9), $(\partial^2/\partial y\,\partial z)(\langle v^2\rangle - \langle w^2\rangle)$, indicates that mean streamwise vorticity is produced by an imbalance between gradients of the wall-normal and free-surface-normal turbulent fluctuations. Perkins (1970) examined turbulent solid–solid corner flows and concluded that secondary streamwise vortices were generated by an imbalance in gradients of normal stresses. Based on Perkins' (1970) work, one can hypothesize a similar mechanism for generating a weak streamwise vortex in the mixed-boundary corner as well.

As with secondary flows in solid–solid corners, the inner secondary vortex is very weak. At any instant of time, it would be masked by turbulence and therefore could not be seen in flow visualization experiments. However, the numerical results clearly indicate that the motion of the inner secondary vortex is directed in toward the wall at the free surface and down away from the free surface at the wall, i.e. counterclockwise as indicated in figure 22.

6.2. *The outer secondary flow*

Experimental results indicate a thickening of the boundary layer close to the surface which cannot be explained by the inner secondary vortex. This thickening was first observed in 1926 by Nikuradse as reported by Schlichting (1979). It is hypothesized that an outer secondary flow transports low-momentum fluid up along the wall, around the inner secondary vortex, and out away from the free surface. This motion is also indicated in figure 22. Visual evidence of this outer secondary motion was provided by the two-colour LIF studies where the laser sheet was placed on the free

surface, figure 8. In those studies, rhodamine dye was always observed moving up along the wall and then away from the wall at the surface. Large-scale motions toward the wall were not observed.

The reader should be aware that the experiments and numerics differ on this point. Numerical results indicate that the outer secondary flow takes the form of a second streamwise vortex which is larger and weaker than the inner secondary vortex. However, the outer secondary flow in the simulations is constrained to be below the inner secondary vortex by the boundary condition at $z^+ = 150$. By contrast, the channel centreline in the experiments is at $z^+ = 3000$; the outer secondary flow is not forced to turn away from the free surface far from the wall.

Turbulence spreading close to the free surface has also been observed in jet and wake flows. The most detailed description of this phenomenon to date appears in Anthony & Willmarth (1992). They used both LIF flow visualization techniques and three-component LDA to study a horizontal turbulent jet issuing into quiescent fluid two jet diameters below a free surface. They documented a thin layer adjacent to the free surface in which the spreading angle of the jet was much greater than the spreading angle of the rest of the jet. Using end view flow visualization, they observed 'puffs' of turbulent fluid which retained their coherence and moved across the free surface. Anthony & Willmarth (1992) conjectured that an ensemble average of these 'puff' motions would yield a net outflow away from the centre of the jet at the free surface.

A similar kinematic explanation for the outer secondary flow in the mixed-boundary corner can be made in the following way. Consider a turbulent burst which has a net motion toward the free surface. On the mean, bursts are oriented in the stream direction. But the motion of any individual burst may have an component in the spanwise direction. Bursts with motion toward the free surface must turn outward away from the wall at the free surface. Thus, low-momentum fluid is transported from the near-wall region below the surface and spread out across the surface. This explains why rhodamine was observed to first appear close to the wall and eject away from the wall in figure 8. A burst with spanwise motion away from the free surface will not affect the free surface.

6.3. *The equilibrium turbulent boundary layer region*

In effect, the inner and outer secondary motions directly result from attenuation of surface-normal fluctuations at the free surface. The inner secondary region was shown to be caused by anisotropy in the wall-normal fluctuations caused by the free surface. The outer secondary flow was due to a turning away from the wall of large spanwise motions at the free surface.

Sufficiently far away from the surface, there obviously should be a region in which turbulence is in a two-dimensional equilibrium (on the mean) state. This is identified as the third region in the turbulent boundary layer/free surface problem. It is unlikely that there is a definitive boundary between the outer secondary region and the equilibrium region. Additional experiments are required to ascertain just how far down free surface effects are felt. Figures 19 and 21 indicate variations in mean and fluctuating quantities 1000 viscous units below the surface.

7. Conclusions

Numerical simulations were conducted in conjunction with experimental flow visualization and single-component LDA measurements to examine the interaction of a turbulent boundary layer formed by flow along a vertical wall with a horizontal free

surface. The motivation for the research is to understand and ultimately model the transport processes in this mixed-boundary flow. The results were carefully examined in the context of mean flow characteristics and turbulent structure. These analyses led to the following conclusions.

Mean flow characteristics:

(i) turbulence in the wall/free surface corner can be divided into an inner secondary region, an outer secondary region, and a two-dimensional equilibrium region;

(ii) the inner secondary region is characterized by a very weak streamwise vortex with flow at the free surface directed in toward the wall and flow along the wall oriented down away from the surface:

(iii) the outer secondary region transports low-momentum fluid up toward the free surface and out away from the wall which thickens the boundary layer at the free surface.

Turbulent structure:

(i) vortices connected to the free surface provide a mechanism for transporting material from the surface to the fluid below;

(ii) spanwise meandering of turbulent wall streaks are inhibited by the free surface; and

(iii) there is a concomitant reduction in streak spacing close to the surface.

Support from the Office of Naval Research through Dr Edwin P. Rood is gratefully acknowledged. L.M.G. and T.W. were supported under Grant no. N00014-92-J-1020 while R.I.L. and J.C.N. were supported under Grant no. N00014-93-WX-24105.

REFERENCES

ANTHONY, D. G. & WILLMARTH, W. W. 1992 Turbulence measurement in a round jet beneath a free surface. *J. Fluid Mech.* **243**, 699.

BRUNDRETT, E. & BAINES, W. D. 1964 The production and diffusion of vorticity in duct flow. *J. Fluid Mech.* **19**, 375.

GESSNER, F. B. 1973 The origin of secondary flow in turbulent flow along a corner. *J. Fluid Mech.* **58**, 1.

GESSNER, F. B. & JONES, J. B. 1961 A preliminary study of turbulence characteristics of flow along a corner. *Trans. ASME* D: *J. Basic Engng* **83**, 657.

GESSNER, F. B. & JONES, J. B. 1965 On some aspects of fully-developed turbulent flow in rectangular channels. *J. Fluid Mech.* **23**, 689.

HANDLER, R. A., SWEAN, T. S., LEIGHTON, R. I. & SWEARINGEN, J. D. 1993 Length scales of turbulence near a free surface obtained from a direct numerical simulation. *AIAA J.* **31**, 1998.

JOHANSEN, J. B. & SMITH, C. R. 1986 The effects of cylindrical surface modifications on turbulent boundary layers. *AIAA J.* **24**, 1081.

KIM, J., MOIN, P. & MOSER, R. D. 1987 Turbulence statistics in fully developed channel flow at low Reynolds number. *J. Fluid Mech.* **177**, 133.

KLINE, S. J., REYNOLDS, W. C., SCHRAUB, F. A. & RUNSTADLER, P. W. 1967 The structure of turbulent boundary layers. *J. Fluid Mech.* **30**, 741.

LAM, K. & BANERJEE, S. 1988 Investigation of turbulent flow bounded by a wall and a free surface. In *Fundamentals of Gas-Liquid Flows* (ed. E. E. Michaelides & M. P. Sharma). ASME Vol. 72, p. 29.

MCLEAN, I. R. 1990 The near wall eddy structure in an equilibrium turbulent boundary layer. PhD dissertation, Dept. of Aero. Engng., University of Southern California.

MOREL, T. 1977 Design of two-dimensional wind tunnel contractions. *Trans. ASME* I: *J. Fluids Engng.* **99**, 371.

NAOT, D. & RODI, W. 1982 Calculation of secondary currents in channel flow. *J. Hydraul. Div. Proc. ASCE* **108**, 948.

ORSZAG, S. A. & PATERA, A. T. 1983 Secondary instability of wall-bounded shear flows. *J. Fluid Mech.* **144**, 721.

PERKINS, H. J. 1970 The formation of streamwise vorticity in turbulent flow. *J. Fluid Mech.* **44**, 721.

ROBINSON, S. K. 1991 The kinematics of turbulent boundary layer structure. *NASA TM*-103859.

SCHLICHTING, H. 1979 *Boundary-Layer Theory*, 7th edn McGraw-Hill.

SMITH, G. B. 1992 Turbulent cascade in colliding off-axis vortex rings. *MS thesis, Dept. of Mech. & Aero. Engng, Rutgers University.*

SPALART, P. R. & WATMUFF, J. H. 1993 Experimental and numerical study of a turbulent boundary layer with pressure gradients. *J. Fluid Mech.* **249**, 337.

STERN, F. 1986 Effects of waves on the boundary layer of a surface-piercing body. *J. Ship Res.* **30**, 256.

STERN, F., PARTHASARATHY, R., HUANG, H. P. & LONGO, J. 1994 Effects of waves and free surface on turbulence in the boundary layer of a surface-piercing flat plate. *1994 ASME Symp. on Free Surface Turbulence, Lake Tahoe, NV.*

SWEAN, T. S., RAMBERG, S. E., PLESNIAK, M. W. & STEWART, M. B. 1989 Turbulent surface jet in a channel of limited depth. *ASCE J. Hydraulic Engng* **115**, 1587.

WEI, T. & WILLMARTH, W. W. 1989 Reynolds number effects on the structure of a turbulent channel flow. *J. Fluid Mech.* **204**, 57.